



Catalytic Decomposition of Methane into Hydrogen and High-Value Carbons: Combined Experimental and DFT Computational Study

Journal:	<i>Catalysis Science & Technology</i>
Manuscript ID	CY-ART-02-2021-000287.R1
Article Type:	Paper
Date Submitted by the Author:	09-May-2021
Complete List of Authors:	<p>Wang, I-Wen; West Virginia University, Chemical Engineering Dagle, Robert; Pacific Northwest National Laboratory, Khan, Tuhin; Indian Institute of Technology Delhi, Chemical Engineering Lopez-Ruiz, Juan; Pacific Northwest National Laboratory, Institute for Integrated Catalysis, Energy and Environment Directorate; Pacific Northwest National Laboratory, Advanced Energy Systems Group, Energy Processes & Materials Division Kovarik, Libor; Pacific Northwest National Laboratory, EMSL Jiang, Yuan; Pacific Northwest National Laboratory, Xu, Mengze; Pacific Northwest National Laboratory, Institute for Integrated Catalysis Wang, Yi; West Virginia University, Department of Mechanical & Aerospace Engineering Jiang, Changle; West Virginia University, Chemical and Biomedical Engineering Davidson, Stephen; Pacific Northwest National Laboratory, Tavadze, Pedram; West Virginia University, Physics and astronomy Li, Li-Li; Zhoukou Normal university Hu, Jianli; West Virginia University, Chemical and Biomedical Engineering</p>

**Catalytic Decomposition of Methane into Hydrogen and High-Value Carbons: Combined
Experimental and DFT Computational Study**

I-Wen Wang^a, Robert A. Dagle^b, Tuhin Suvra Khan^c, Juan A. Lopez-Ruiz^b, Libor Kovarik^b,
Yuan Jiang^b, Mengze Xu^b, Yi Wang^d, Changle Jiang^a, Stephen D. Davidson^b, Pedram
Tavadze^e, Lili Li^{f,*}, and Jianli Hu^{a,*}

^a Department of Chemical & Biomedical Engineering, West Virginia University, Morgantown, WV 26506, USA.

^b Institute for Integrated Catalysis, Pacific Northwest National Laboratory, 902 Battelle Blvd Richland, WA 99352, USA.

^c Light Stock Processing Division, CSIR-Indian Institute of Petroleum, Dehradun 248005, India.

^d Department of Mechanical & Aerospace Engineering, West Virginia University, Morgantown, WV 26506, USA

^e Department of Physics, West Virginia University, Morgantown, WV 26506, USA

^f College of Life Science and Agronomy, Zhoukou Normal University, Zhoukou, Henan, China

*Corresponding authors: Tel: (304)293-5067. Email: john.hu@mail.wvu.edu;

Tel: (86)13672165360. Email: 13672165360@163.com

Abstract

Thermocatalytic decomposition (TCD) of methane can produce hydrogen and valuable nanocarbon co-products with low to near-zero CO₂ emission. In this study, a series of Pd promoted Ni catalysts, prepared with varying Ni/Pd ratio on CNT support, were evaluated for methane TCD performance. Characterization and calculation by Density Functional Theory (DFT) were carried out to elucidate activity-structure relationship and growth mechanism of carbon nanomaterials. It was found that methane conversions and stability of the catalysts were highly dependent on the Ni/Pd ratio and reaction temperature. DFT calculation revealed that the diffusion of carbon in the metal sublayer required for CNT growth was more favorable in the Ni-Pd alloy lattice suggesting that the buildup of carbon in the metal alloy sublayer facilitated the formation of CNT and CNF. A cyclic reaction-regeneration process for self-sustained TCD was experimentally demonstrated. In each cycle, a portion of the separated CNT product was used to re-synthesize Ni-Pd/CNT catalyst for the use in the next reaction cycle. After five cycles of operation, CH₄ conversion, morphology and crystallinity of carbon product remained unchanged.

Keywords: Carbon nanomaterials production; Thermocatalytic methane decomposition; Self-sustained process with recyclable catalyst; Density functional theory; CO₂-free hydrogen production.

1. Introduction

Hydrogen, an energy carrier with high conversion efficiency and zero carbon emission, is receiving unprecedented support government and broad industrial sectors. However, the vast majority of the world's H₂ supply is produced from fossil fuels thereby resulting in CO₂ emissions. For example, about 96% of global H₂ (48% in the United States) is produced via steam methane reforming (SMR), leading to an average emission of 10 kg CO₂/kg H₂.^{1,2} Therefore, owing to environmental and potential future regulatory concerns it is desirable to develop a process for near-zero CO₂ production of H₂ and one that is economically viable.

Renewable energy, such as solar-assisted water electrolysis, is clean and sustainable for high-purity H₂ production. However, the unpredictable energy resource and dependence on stable power grid are the challenges to overcome.^{3,4} Hydrogen production from biomass via bi-photolysis, fermentation and gasification were reported but suffered from low H₂ production rates and yields.^{5,6}

In contrast, TCD of methane proves to be a promising option during because of its characteristics of efficient production of H₂ and valuable solid carbon.⁷⁻⁹ The commercial viability of the TCD process is highly dependent on the efficiency, stability and regeneration of the catalyst. With respect to catalyst development, many possible mono- and bi-metallic and carbonaceous catalysts have been reported with morphological features being studied.^{10,11}

Catalyst supports investigated include various metal oxides and carbon while unsupported catalysts are of interest as well.^{12,13} The studies were carried out on the selection of metals, catalyst supports^{14,15} and the methods of catalyst preparation.^{16,17} Thermo-catalytic decomposition of methane to CO_x-free hydrogen and valuable carbon materials has been reviewed.^{18,19} Chen et al.²⁰ has conducted a kinetic study for thermo-catalytic decomposition of methane using electroless Ni plating catalyst at 525-600 °C. The results showed that the reaction order was 2 and the activation energy for this specific reaction was 113.993 kJ/mol. The study further found out that the deactivation order was 0.5 and the deactivation energy was 147.870 kJ/mol. In addition, molten salts were studied for methane reforming, which might be considered for methane decomposition.^{21,22} Kang et al.²³ has shown that the Fe containing molten salts (NaCl-KCl) catalyzed the methane decomposition into graphitic solid carbon and H₂ in a bubble column reactor. It was also reported that a bubble column reactor containing liquid or vapor tellurium was able to facilitate the methane pyrolysis.²⁴ Although there was mechanistic studies on the formation of carbon nanomaterials over metal supported catalysts,^{20,25} the in-depth investigation using density functional theory (DFT) for the CNT supported binary metal catalyst is worth investigating.²⁶⁻²⁸ As a part of this study, DFT modeling work was carried out to study the TCD mechanism over Ni-Pd catalysts.

A forward movement of TCD commercialization seems not very effective because few works have been focused on TCD-based processes that represent industrial practice. Many researchers

were trying to solve catalyst stability issues by developing new catalytic materials. However, a catalyst with everlasting activity might not be urgently needed because an industrial TCD process may need a cyclic regeneration configuration where TCD is operated in a continuous reaction-regeneration mode. In such an operating mode, separation of carbon from the solid catalyst would need to take place at certain time-on-stream of TCD. Therefore, the commercialization strategy is to carry out in-process catalyst-carbon separation and regeneration as practiced in petroleum refinery.

Effective catalyst-carbon separation and catalyst regeneration are major challenges to the success of TCD commercialization. Mechanical separation by attrition method was examined in a fluidized-bed reactor but the separation efficiency was low.²⁹ The use of carbon catalysts seemed to be able to eliminate carbon product separation step.³⁰ However, the activity of carbon catalyst gradually declined and without oxidized regeneration its activity would not be recovered.³¹ Acid treatment is commonly used for separation and purification of grown CNT from catalysts,³² while both oxide support and metal on the support are dissolved in acid making metal recovery difficult.

In this study, a TCD process consisting of cyclic reaction-regeneration was experimentally demonstrated where Ni-Pd/CNT catalyst could be regenerated and re-used. As illustrated in Figure 1, after TCD reaction, separation of carbon products (CNT/CNF) and catalyst was

accomplished by using acid to dissolve Ni-Pd, leading to metal-free CNT. The acid-leached Ni-Pd was recovered and re-used. In the regeneration step, a portion of carbon product (i.e., CNT/CNF) was used as catalyst support, and the catalyst was re-synthesized using recovered Ni-Pd. The objectives of this study were to study the growth mechanism of CNT/CNF over supported Ni-Pd catalysts and demonstrate the feasibility of cyclic regeneration for potential commercial application.

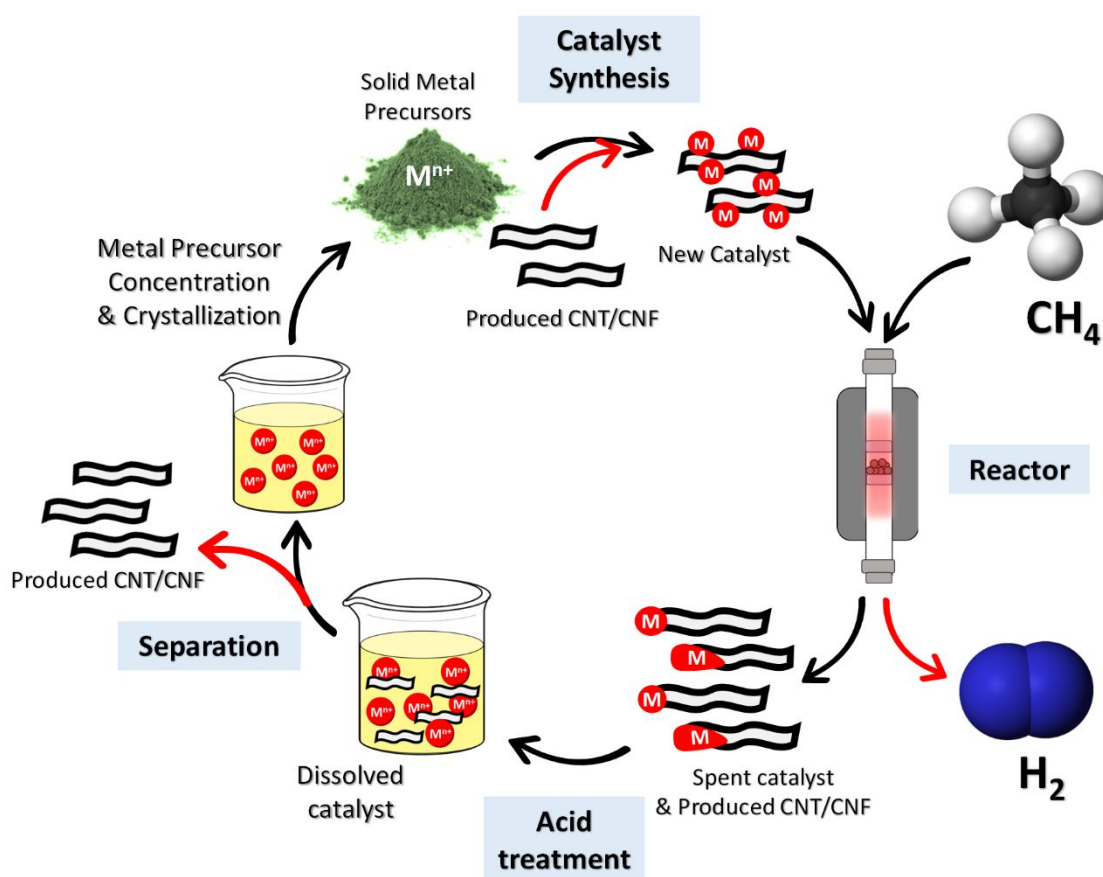


Fig. 1. Illustration of the proposed cyclic methane TCD process consisting of TCD reaction, catalyst-carbon separation, and catalyst regeneration steps.

2. Experimental and DFT calculation methods

2.1. Catalyst preparation.

The monometallic and bimetallic catalysts containing a total amount of 11 wt% metal on CNT (X of Ni : 1Pd) were prepared via a solvothermal method. The weight ratio of metal is designed as X of Ni : 1 Pd for supported and unsupported catalysts. For example, 10Ni-1Pd/CNT means Ni loading is $(10/11) \times 11$ wt% total metal and Pd loading is $(1/11) \times 11$ wt% total metal over 89 wt% of CNT; unsupported 15Ni-1Pd means catalysts with 15/16 wt% of Ni and 1/16 wt% of Pd. The precursors of $\text{Ni}(\text{NO}_3)_2 \cdot 6\text{H}_2\text{O}$ (Acros Organics, 99%) and $\text{Pd}(\text{NO}_3)_2 \cdot 2\text{H}_2\text{O}$ (Sigma-Aldrich, ~40% Pd basis) were dissolved in 50 ml acetone (Fisher Scientific, Certified ACS) under agitation for 1 hr and sonicated for 25 minutes before CNT (Cheap tubes Inc., >95%) was added into the solution. The solution was continuously stirred for 3 hr and subsequently sonicated for 30 min. The resulting solution was transferred into a Teflon-lined stainless-steel autoclave (100 ml), sealed and heated to 120 °C for 12 hr. After the autoclave was cooled to room temperature, the solution from autoclave was placed inside a fume hood to evaporate acetone solution at room temperature and subsequently dried overnight at 80 °C until completely dry. Dry solids were ground into fine powders, reduced at 400 °C for 4 hr in a tube furnace using 10 mol% H_2 in N_2 (H_2 : 99.999%; N_2 : 99.999%) at 50 ml/min, and stored in a vacuum desiccator. The unsupported catalysts were prepared following the same protocol.

2.2. Catalyst preparation for cyclic reaction-regeneration test.

After the first cycle reaction, the spent catalyst was refluxed with 3.0 M HNO₃ (Fisher Scientific, Certified ACS Plus) at 120 °C for 4 hr and concentrated HNO₃ at 130 °C for 12 hr under continuous agitation. After the acid digestion, the carbon particles were filtered, washed with deionized water, and dried at 80 °C under stagnant air. A portion of the product carbon was used to synthesize the catalyst for the next cycle. The catalyst synthesis protocol (i.e., metal deposition, drying, and reduction) used to generate the catalyst for the following cycles was the same as the fresh catalyst.

2.3. Catalytic activity measurements.

CH₄ TCD reaction was performed using a vertical fixed-bed reactor with a quartz tube (i.d. = 10 mm, o.d. = 12 cm, and length = 44.5 cm) and heated by an electric tubular furnace (Applied Test System Inc.). The reaction temperature was measured by a K-type thermocouple located above the catalyst bed. The total feed gas flow rate was set at 30 ml/min consisting of 30 mol% CH₄ in N₂. For each test, the amount of reduced catalyst used was 0.2 g, and the reactor was purged by N₂ at 70 ml/min and heated to 120 °C for 30 min. Then the tests were conducted at temperatures between 500 and 700 °C with a ramping rate of 10 °C /min. The composition of outflow gas was analyzed by a 4-channel Fusion Micro GC manufactured by INFICON Inc.

Under reaction conditions, the CH₄ conversion (%) and H₂ selectivity were described as follows in Eq. 1 and Eq. 2.

$$\text{CH}_4 \text{ conversion (\%)} = (1 - (\text{CH}_4^{\text{out}} N_2^{\text{in}} / \text{CH}_4^{\text{in}} N_2^{\text{out}})) * 100\% \dots \text{Eq. 1}$$

Where CH₄^{out} and CH₄ⁱⁿ were the mole concentration of CH₄ outlet and inlet, respectively and N₂^{out} and N₂ⁱⁿ were the mole concentration of N₂ outlet and inlet, respectively.

$$\text{H}_2 \text{ selectivity} = (\text{H}_2^{\text{out}} \times N_2^{\text{in}} / (2 \times \text{CH}_4^{\text{in}} \times N_2^{\text{out}} \times \text{CH}_4 \text{ conversion})) \dots \text{Eq. 2}$$

Where H₂^{out} was the mole concentration of H₂ outlet.

2.4. Characterizations of catalyst.

X-ray diffraction (XRD) was performed with a PANalytical X'Pert Pro X-ray Diffractometer using Cu- α source (45 kV and 40 mA). The morphology of catalysts and produced carbon nanomaterials were analyzed with a transmission electron microscopy (TEM). The TEM images were performed on a JEOL JEM-2100 and worked at an accelerating voltage of 200 kV. The sample preparation was done by sonicating in acetone solution for 15 min. After that, a few drops of suspension were dropped onto the TEM grid for analysis. The Energy-dispersive x-ray spectroscopy (EDS) in scanning transmission electron microscopy (STEM) was used to map the distribution of metal elements on particles. The STEM imaging was performed on an aberration-corrected Titan 80-300 apparatus at an accelerating voltage of 200 kV. The scanning

electron microscopy (SEM) images were conducted on Hitachi S-4700. The thermal stability and purity of the catalysts were studied by thermogravimetric analysis (TGA) on a TA Instruments SDT 650 analyzer. The maximum temperature reached was 900 °C with a heating rate of 10 °C/min. Gas mixture used in the TGA analysis contained 5 mol% O₂ in He (Airgas) with a flow rate of 100 SCCM. The Raman spectroscopic analysis was performed in a Renishaw InVia Raman Microscope with an excitation wavelength of 532 nm.

2.5. DFT calculation methods

Binding energies of intermediates were calculated using Vienna ab initio simulation package (VASP-5.3.5version, University of Vienna) DFT code.³³ Plane wave basis function was used to describe the Kohn Sham one electron valence states, whereas the core-electrons were described using the Vanderbilt ultrasoft pseudopotentials.³⁴ An energy cut-off of 396 eV was used for the plane-wave basis functions. The GGA Revised Perdew-Burke-Ernzerhof (RPBE) exchange-correlation functional developed by Hammer et al.³⁵ was used for all the calculations.

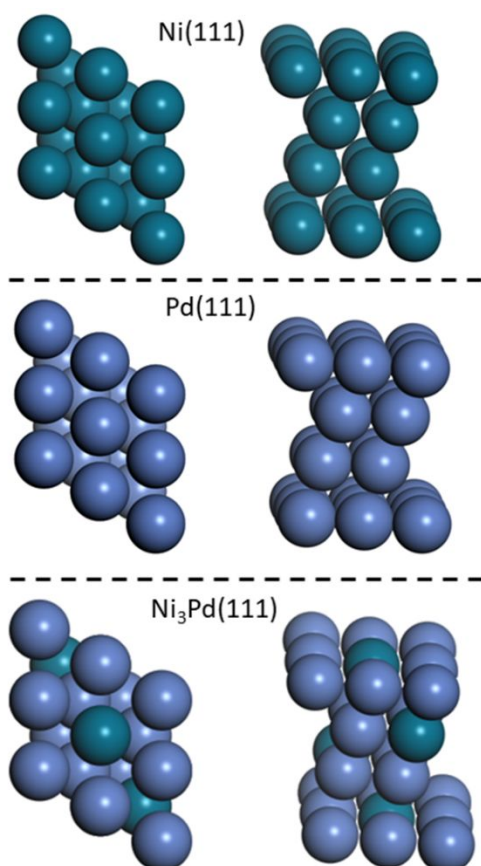


Fig. 2. Density functional theory (DFT) model of the optimized structure of Ni(111), Pd(111) and Ni₃Pd(111) catalyst model surfaces.

The bimetallic Ni-Pd alloy is modelled using Ni₃Pd alloy FCC crystal geometry. Lattice optimization of the Ni₃Pd crystal is performed to get the correct lattice parameter $a=b=c=3.71$ Å, $\alpha = 90^\circ$. Terrace (111) surface of Ni, Pd, and Ni₃Pd modelled using a slab of 4 layers of size 4 x 4. Bottom two layers of the surface slab are kept fixed while the upper half along the adsorbates are allowed to relax, as has been shown in Fig. 2. A vacuum of 20 Å is added along the z-axis between the slabs to represent the adsorption of gas-phase species to the metal surface. A 3 x 3 x 1 Monkhorst-Pack³⁶ k-point grid is used for the irreducible Brillouin zone.

The force and energy convergence criteria are set to 0.05 eV/Å and 10^{-4} eV, respectively. All the calculations performed for Ni (111) and Ni₃Pd (111) surfaces were spin-polarized. Methfessel-Paxton³⁷ smearing parameter of value 0.2 is used for all the calculations. The (111) closed packed terrace is the most abundant surface having ~ 75% surface area. Sanchez-Valencia et al. have experimentally produced (6,6) CNT over a Pt (111) surface.³⁸ The (111) terrace surface was used by Harpale et al.,³⁹ Elliott et al.,⁴⁰ and Gili et al.⁴¹ to study the CH₄ to graphene and CNT/CF formation over Ni catalyst under CVD condition. The preferential growth of the CNT/CF over the (111) surface can be attributed to the symmetry match between the metal (111) surface and the graphene layer, with both having hexagonal C₆ symmetry.²⁷

3. Results and discussion

3.1. Physiochemical properties and morphology of Ni-Pd alloy catalysts

The Ni/Pd ratio was varied for both unsupported and CNT-supported catalysts to investigate the effects of support and metal composition. Fig. 3a presents the XRD results of as-reduced Ni-Pd-CNT catalysts with different Ni/Pd ratios. The XRD patterns of CNT, Pd/CNT, and Ni/CNT show their characteristic peaks confirming their crystalline structures, according to their standard XRD patterns in Fig. S1. The XRD spectra of 10Ni-1Pd/CNT, 5Ni-1Pd/CNT, and 1Ni-1Pd/CNT show similar patterns with that of Ni/CNT, indicating that these bimetallic particles are well-crystallized forming a Ni-based Ni-Pd alloy lattice.⁴² With the addition of

Pd, the two main peaks corresponding to the fcc Ni lattice shift to lower angles from 44.5° (Ni/CNT) to 42.9° (1Ni-1Pd/CNT), suggesting that the lattices of bimetallic catalysts are enlarged due to the larger atomic radius of Pd as compared with Ni. The same phenomenon in diffraction can also be observed for the as-reduced and spent unsupported Ni-Pd catalysts which are shown in Figs. S1 and S2. Illustrated in Figs. 3b and S3 are the STEM-EDS mappings of the spent unsupported 10Ni-1Pd and 10Ni-1Pd/CNT catalysts on which Ni and Pd atoms are well-dispersed throughout the metallic particle. This agrees with the XRD results and further proves the Ni-Pd alloy formation.

Fig. 3 (c-f) depict TEM images of the fresh catalysts which show that the metal particle size and morphology are affected by both the presence of a support (CNT) and Pd content. First, the use of CNT support causes the decrease of average metal particle size. For example, the fresh 10Ni-1Pd/CNT (Fig. 3c) shows a narrow metal particle size distribution with an average size of 18 nm, while the unsupported 10Ni-1Pd catalyst (Fig. 3d) consists of agglomerates composed of around 50 nm metal particles. Moreover, the addition of Pd causes a decrease of metal particle size for the CNT-supported catalysts, which is consistent with literature reports.^{43,44} Fig. S4 shows that metal particle distribution of the fresh Ni/CNT is bimodal and has an average particle size of ≈ 44 nm, while for the 1Ni-1Pd/CNT, the particle size distribution narrows down and the average particle size decreases to ≈ 9 nm. As shown in Fig.

S5 SEM images, severe sintering of microparticles is found over the unsupported Ni (Figs. S5 a and b), while less sintering is observed over 15Ni-1Pd (Figs. S5 c and d) and spherical nanoparticles can be clearly observed on the 10Ni-1Pd (Figs. S5 e and f).

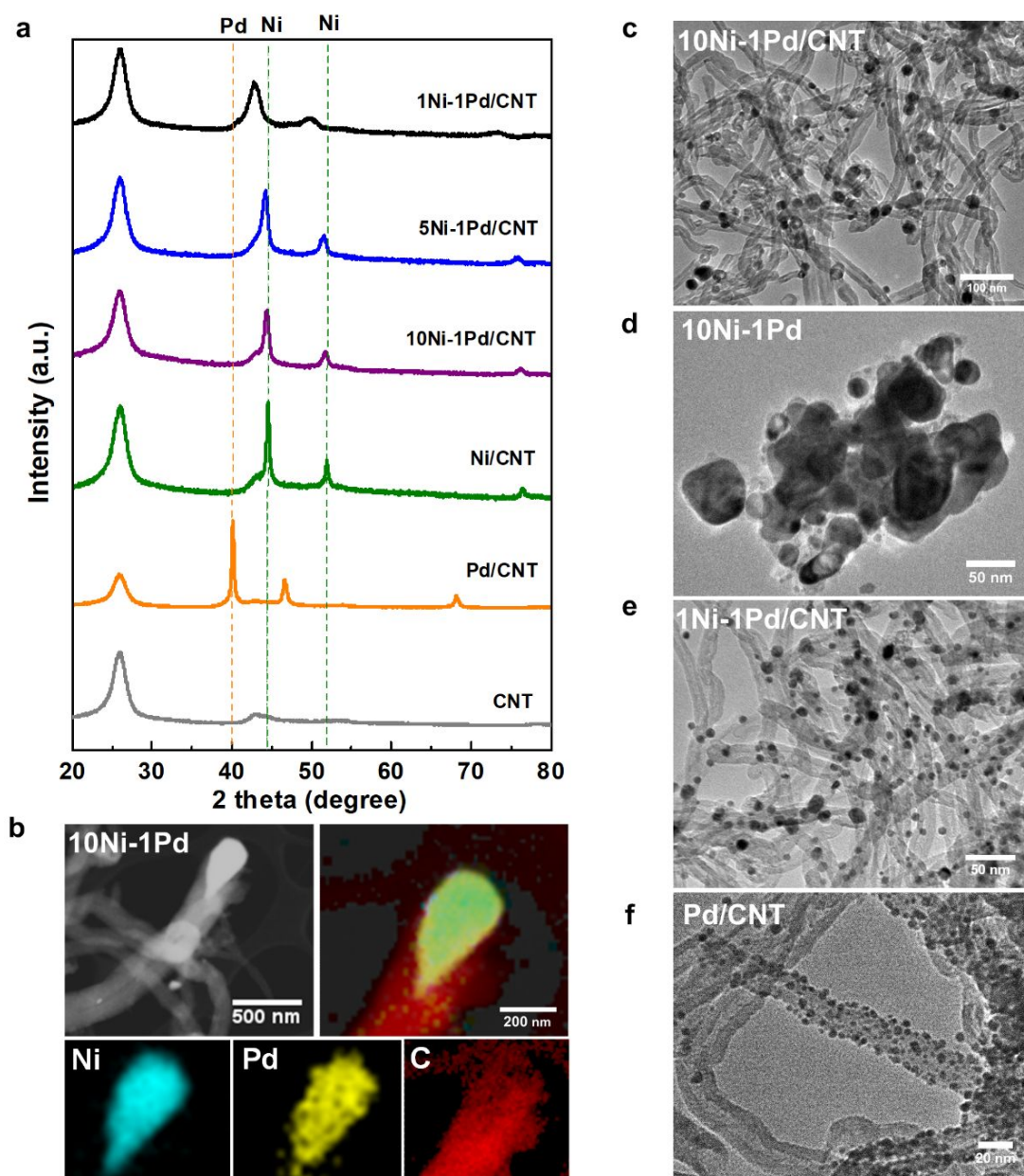


Fig. 3. a) XRD patterns of the fresh (reduced) CNT-supported Ni-Pd catalysts. **b)** STEM-EDS mapping of spent unsupported 10Ni-1Pd. **c-f)** TEM images of fresh (reduced) catalysts. The CNT-supported

catalysts and unsupported catalysts were prepared via the same solvothermal method. The weight ratio of metal is designed as X of Ni:1 Pd catalysts. For example, 20Ni-1Pd/CNT means that Ni loading is $(20/21)*11$ wt.% total metal and Pd loading is $(1/21)*11$ wt% total metal over 89 wt.% of CNT; unsupported 15Ni-1Pd means catalysts with 15/16 wt.% of Ni and 1/16 wt.% of Pd.

3.2. Performance of Ni-Pd catalysts in methane TCD

Catalytic performances of the supported and unsupported Ni-Pd catalysts in TCD are shown in Fig. 4. As illustrated in Fig. 4a, CNT-supported and unsupported Ni catalysts deactivate rapidly within 2 hr. The rapid deactivation is due to the formation of graphitic layer on Ni particles which are confined by TEM measurement and DFT modeling work shown in the following sections. Upon the addition of Pd (0.52 wt.%, 20Ni-1Pd/CNT), methane conversion remains stable for 6 hr. An optimum Pd loading is found to be between 0.52 wt.% and 1.8 wt.% for the CNT-supported catalysts, which corresponds to 20Ni-1Pd and 5Ni-1Pd, respectively. Further increase in Pd loading is detrimental to the catalytic activity (e.g., 1Ni-1Pd/CNT). Similarly, the unsupported catalysts also show high and stable performance with an optimum Pd loading between 10Ni-1Pd and 5Ni-1Pd (Fig. 4a, Zone IV). It is noted that the use of CNT significantly decreases requirement on total metal loading from 100 wt.% to 11 wt.%. Fig. 4b summarizes the TCD activity as a function of Ni : Pd mass ratio for both CNT-supported and unsupported catalysts. The data were taken at 1 hr time-on-stream. The use of CNT-support improves metal

particle dispersion whereas the addition of Pd to Ni helps to stabilize metal particles and inhibit the termination of the CNT growth due to coking.^{45,46} More detailed discussion on TCD mechanism is presented in the DFT modeling work in the following section.

Fig. 4c depicts the effect of reaction temperature on the stability of the 10Ni-1Pd/CNT. The activity remains stable for over 6 hr when the reaction temperature is lower than 600 °C but deactivates within 1 hr when the reaction temperature is over 650 °C. At temperatures above 650 °C, the pure nickel catalyst was deactivated due to the fact that methane dissociation rate was faster than carbon diffusion rate, resulting in the encapsulation of nickel particles by graphitic layers.^{47,48} Fig. 4d shows the catalytic activity of 10Ni-1Pd/CNT with the varying CH₄ molar fraction from 30% to 100% at 600 °C. Although the conversion decreases with the increase in CH₄ concentration, hydrogen production rate increases indicating the CH₄ conversion rate (mole CH₄ converted/hr) is increasing. Even at 100% concentration of methane, the methane conversion remains stable at 35%.

The feasibility of cyclic reaction-regeneration as described in Fig. 1 was examined using 10Ni-1Pd/CNT catalyst. Fig 4e depicts the catalytic stability of 10Ni-1Pd/CNT for five cycles of operation. Fig. 1 shows one complete cycle. In each cycle, a portion of carbon product (CNT/CNF) was taken after leaching out Ni-Pd by nitric acid. Ni and Pd are re-introduced using fresh Ni-Pd nitrate. Practically, we could use Ni-Pd nitrate solution from acid wash, but

the evaporation took long time in laboratory setting. It is worth noting that the solubility of multi-walled CNTs in nitric acid was considered low. In each cycle, we took a fraction of product carbon as support to reload metals. During the TCD, these carbon supports were mixed with new carbon product and diluted. The amounts of carbons that undergo repeatedly acid wash were less. Results shown in Fig. 4e indicate that the catalytic activity can be recovered after each cycle of regeneration. Although the concept of using the as-produced CNT product as support for making catalyst was mentioned in a literature,¹⁰ to the best of our knowledge, this is the first reporting that experimentally demonstrates the feasibility of in-process catalyst regeneration for self-sustained TCD process. The properties of CNT/CNF from cycles 1, 3 and 5 are described in next section. Our experiment was carried out in fixed-bed configuration using quartz tube reactor. Typically, the pyrolysis reaction was operated for six hours when pressure started to build up. However, if bubbling bed reactor were used, the catalytic pyrolysis could be operated for much longer time. The long operation duration is important for commercial practice, it saves capital and operating costs.

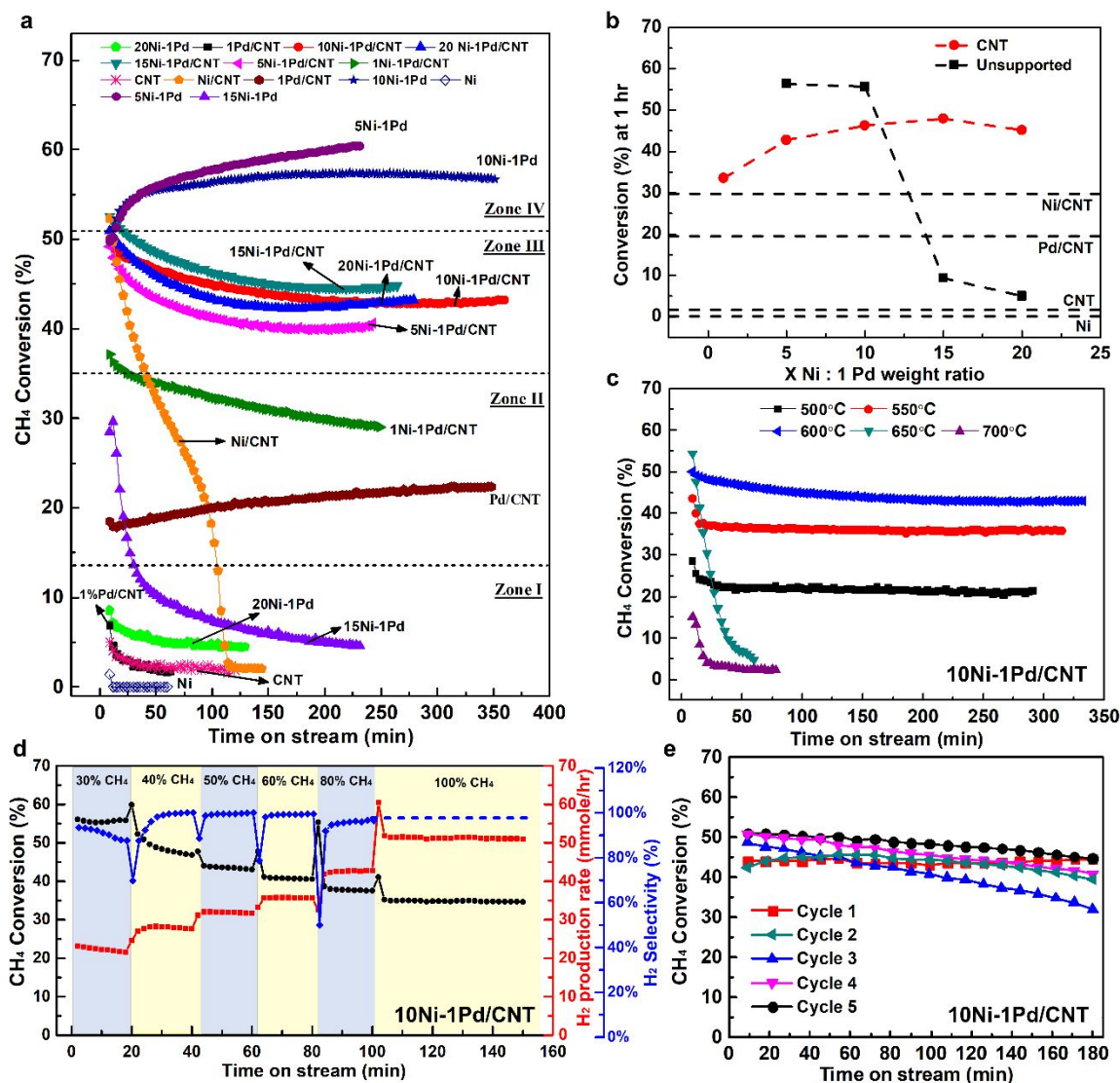


Fig. 4. a) CH₄ conversion over CNT-supported and unsupported catalysts with different Ni-Pd mass ratio. TCD reaction conditions: 600 °C, 30 mol% CH₄/N₂. The graph is divided into four zones based on conversion values of catalysts, from low to high. b) CH₄ conversion as a function of Ni:Pd mass ratios at 1 hr time-on-stream c) Effect of temperature on CH₄ conversion on 10Ni-1Pd/CNT. d) Effect CH₄ molar fraction in feedstock on catalyst performance operated at 600 °C. e) Feasibility test of cyclic reaction-regeneration for 5 cycles.

3.3. Characterization of spent catalyst and carbon products

The morphologies of the spent Ni/CNT and 10Ni-1Pd/CNT catalysts are depicted in Figs. 5 (a-c). Shown in Fig. 5a is the coke formation on Ni particles over Ni/CNT catalyst, which explains the rapid deactivation of Ni/CNT in TCD (Fig. 4a). The carbon product on Ni/CNT appears to be multi-walled CNT which appears to be hollow cylindrical shape. For CNT-supported Ni-Pd alloy catalysts, the carbon products consist of mainly CNF as shown in Figs. 5 b and c. Fig. 5c shows spent catalyst taken from 5th cycle. This sample contains CNT products taken from previous 4 cycles. Results from Fig. 5c indicate that the CNF formed from each cycle does not show any obvious difference in morphology.

It is worth noting that, in the Ni-Pd-CNT catalyst system, very small metal particles do not tend to show catalytic activity. Fig. S6 shows that spent 10Ni-1Pd/CNT and Pd/CNT with the particle size less than its critical value do not grow CNT or CNF. In contrast, larger Ni-Pd particles produces large CNF as shown in Fig. S6b. One explanation is that, compared with larger particles, the deactivation over small particles is due to the “overfeeding” of carbon atoms from CH₄ which causes thin carbon layer formation on the surface preventing further CNT nucleation.⁴⁹ Fig. S7 shows the SEM images of spent unsupported Ni, 10Ni-1Pd and 15Ni-1Pd catalysts. Fig. 8S illustrates Raman spectra of unsupported Ni-Pd catalysts.

The crystallinity of the produced carbon was examined using Thermogravimetric analysis (TGA). Fig. 5d shows that the oxidation temperatures of the CNT-supported catalysts are higher than 500 °C, implying that the produced carbon is crystalline because amorphous carbon is oxidized at a temperature less than 400 °C. Raman spectroscopy was used to determine the degree of crystallinity of the produced carbon by monitoring the ratio between the D-band (1345 cm⁻¹) and G-band (1578 cm⁻¹).⁵⁰ As shown in Fig. 5e, the I_D/I_G ratios are between 1.4 and 1.6 for CNTs recovered from cycles 1, 3 and 5, indicating the reaction-regeneration cycles do not affect the crystallinity of carbon products.

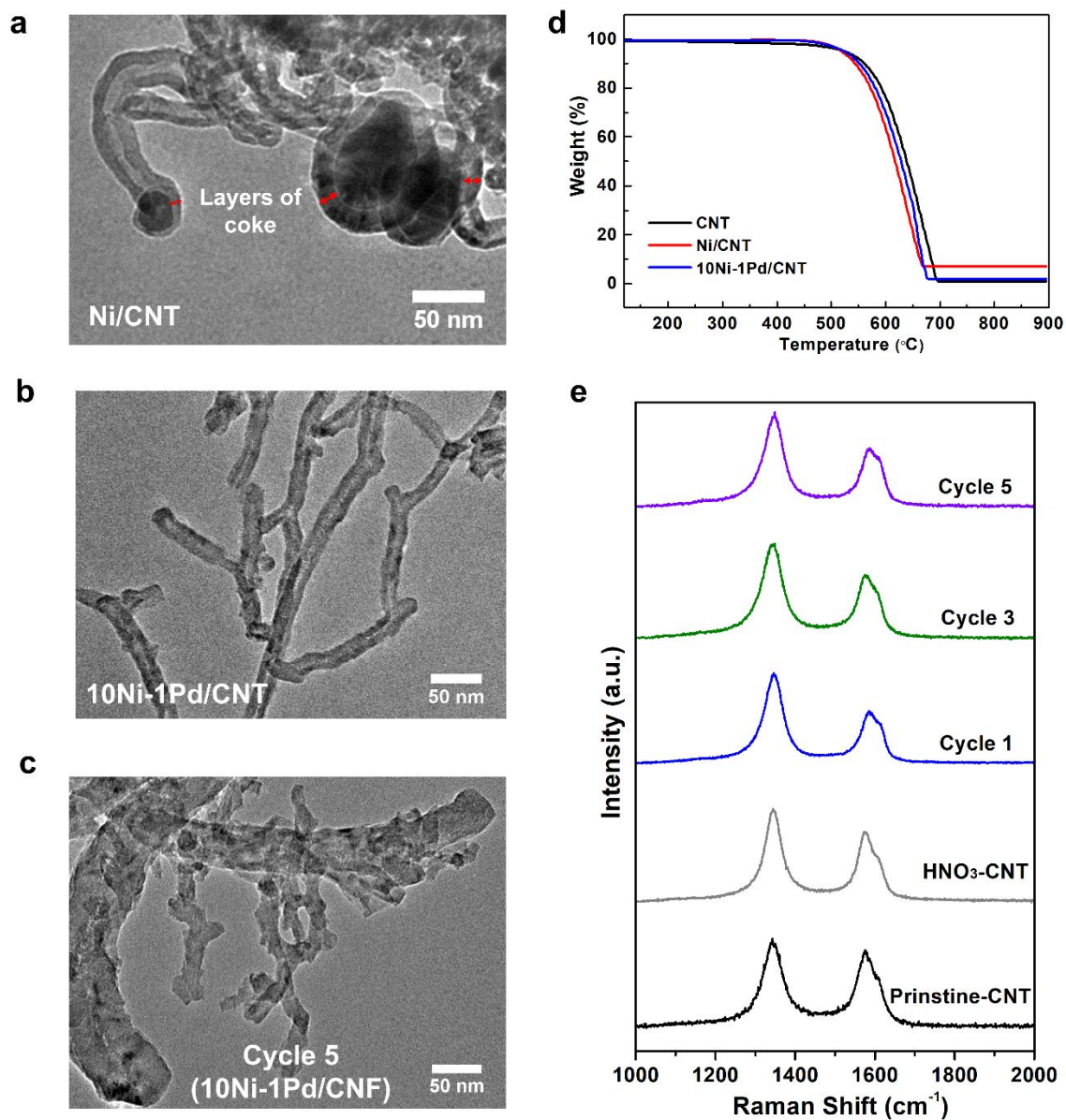


Fig. 5. **a)** TEM image of coke formation over Ni/CNT. **b)** TEM image of thick-walled CNT and CNF over 10Ni-1Pd/CNT. **c)** CNF after 5th cycle. **d)** TGA analysis with oxidation temperature up to 900°C. **e)** Raman patterns of the pristine, acid treatment CNT and the spent catalysts after the 1st, 3rd, and 5th cycles.

3.4. Mechanistic understandings from the computational investigation

To understand the role of Pd in the Ni-Pd bimetallic system for the varied catalytic activity, Ab-initio microkinetic modeling (MKM) in conjunction with Density functional theory (DFT) was applied to investigate intrinsic CH₄ decomposition rates over Ni, Ni₃Pd, and Pd (among other metals). More information about the DFT and MKM methods can be found in the Supplementary Information.

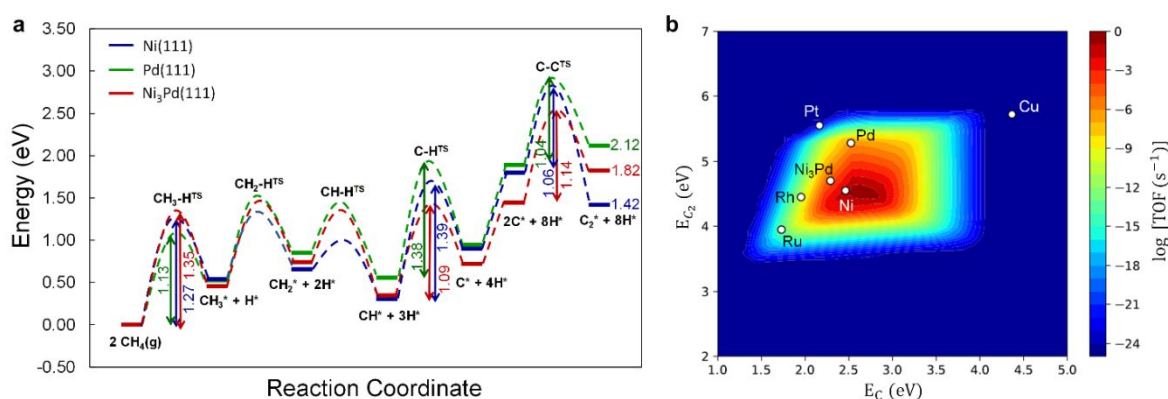


Fig. 6. a) Potential energy diagram for the CH₄ TCD and C₂ formation over Ni(111), Pd(111) and Ni₃Pd(111) surfaces. **b)** Contour plot for CH₄ TCD over transition metal surfaces plotted against the two MKM descriptors, C and C₂ binding energy. Reaction conditions were 600 °C, 1 bar CH₄, and conversion of 0.01%. The binding energies and transition state scaling relationships used in the models are shown in Fig. S9. Detailed discussion about the DFT and MKM modeling can be found in Supplementary Information.

Fig. 6a shows the activation energy barrier of breaking four C-H bonds and C₂ formation over Ni, Ni₃Pd, and Pd surfaces. As can be seen in Fig. 6a, all three catalyst surfaces have similar

energy profiles with similar activation barriers for C-H bond dissociation and C-C coupling reaction. However, the formation of C₂ species (C₂ +8H) is more favorable over the Ni(111) surface (1.42 eV), compared to the Pd(111) and Ni₃Pd(111) surface (2.12 eV and 1.82 eV, respectively). Incorporating the DFT data of energy barrier of each step, Fig 6b plots MKM results of the activity as a contour plot, using the binding energies of C and C₂ species as the two descriptors.^{51,52} Among all the metals, Ni is the most active with TOF ~ 0.1 s⁻¹; however, Ni₃Pd and Pd are ≈ 3 and 5 orders of magnitude less active, TOF ~ 10⁻⁴ and ~ 10⁻⁶ s⁻¹, respectively. This calculation reflects intrinsic kinetics.

To understand the higher stability of Ni-Pd alloy catalysts towards coke formation compared to Ni, DFT modeling work was carried out. As previously shown, though Ni/CNT shows the highest initial methane conversion, it deactivates very quickly due to coke formation, whereas Ni-Pd-CNT catalyst shows stable conversion of methane for ~ 6 hrs. While the C₂ formation is considered the precursor for carbon encapsulation (i.e., active site deactivation) and coke formation, the dissolution and migration of surface atomic carbon in the metal sublayer is considered the key step towards the formation of CNT/CNF⁵³⁻⁵⁶ and the stability. Therefore, we evaluated over Ni and Ni₃Pd (111) surfaces using DFT modeling to calculate energies for atomic carbon dissolution and C₂ formation to unravel the role of Pd.

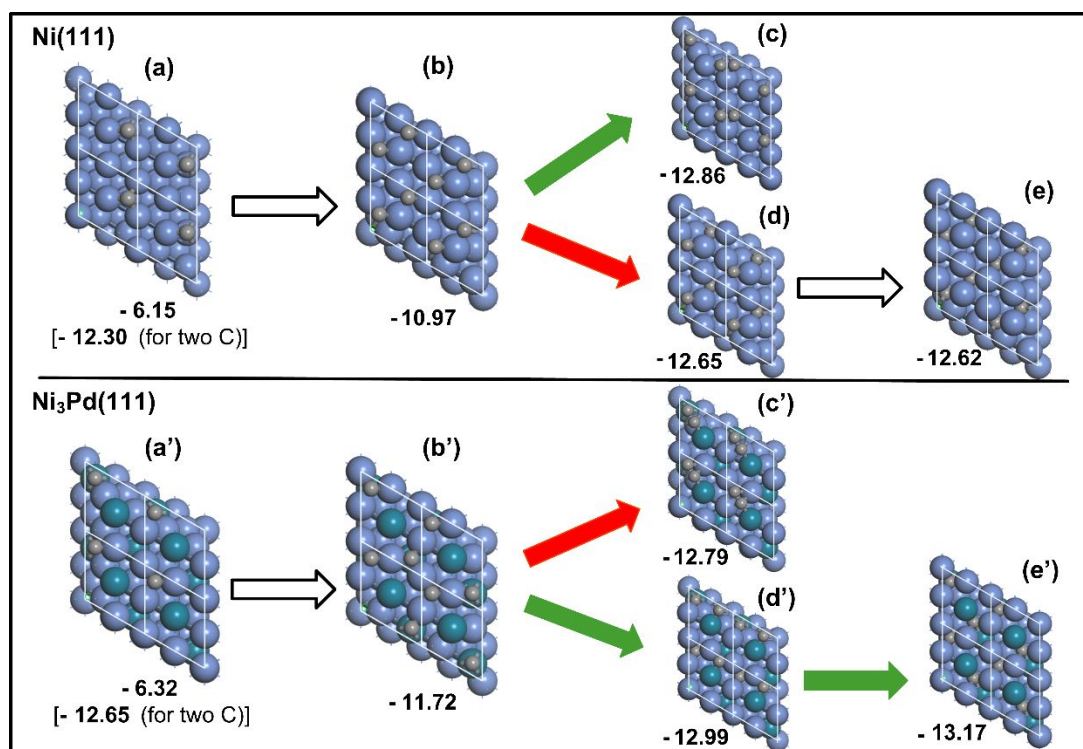


Fig. 7. DFT calculated energies for the competing routes for C₂ formation vs. the dissolution of carbon over Ni(111) [top] and Ni₃Pd(111) [bottom] surfaces. Favorable route marked with green arrow. All the binding energies given below the geometries are in eV. More information about the calculations of the formation and diffusion energies can be found in the Supplementary Information (Section S2).

As shown in Fig. 7, the carbon atoms bind strongly to both the Ni(111) and Ni₃Pd(111) surfaces with similar binding energy -6.15 eV (Fig. 7a) and -6.32 eV (Fig. 7a'), respectively. At higher coverage 0.5 ML, the binding energy of two carbon over Ni(111) and Ni₃Pd(111) are calculated to be -10.97 eV and -11.72 eV, respectively (Figs. 7 b and b'). Due to the high reaction temperature and high methane gas concentration, reasonably high coverage of C is expected on the metal surfaces. These two carbons adsorbed at the surface can either undergo C-C

coupling to form C_2 species (Figs. 7c and 7c' for Ni and Ni_3Pd , respectively), or they can diffuse to the sub-layer of the metal surface (Figs. 7 (d \rightarrow e) and 7 (d' \rightarrow e') for Ni and Ni_3Pd , respectively). The diffusion of carbon from the surface to the sublayer is energetically favorable for both Ni and Ni_3Pd by -1.68 eV (Fig. 7b \rightarrow 7d) and -1.27 eV (Fig. 7b' \rightarrow 7d'), respectively. A similar observation was made by Albid-Pedersen et al.,⁵⁷ Harpale et al.,³⁹ and Gili et al.⁴¹ The energy gain from the diffusion of the second carbon to the first sublayer is favorable only by -0.18 eV for Ni_3Pd (Fig. 7d' \rightarrow 7e'), whereas it is unfavorable for Ni ($\Delta E = +0.03$ eV, Fig. 7d \rightarrow 7e). The diffusion of carbon from first sublayer to the second sublayer were found to be unfavorable for both Ni(111) and $Ni_3Pd(111)$ by 0.25 eV and 0.09 eV, respectively, as shown in Fig. S10.

The formation of C_2 from the surface adsorbed C atoms is more energetically favorable for Ni at -1.89 eV (Fig. 7b \rightarrow 7c) than for Ni_3Pd at -1.07 eV (Fig. 7b' \rightarrow 7c'). These results suggest that the formation of graphitic layers on the Ni surface is more favorable, which is consistent with our stability and characterization results that show the pure Ni particles covered by graphitic layers. However, the diffusion of C in the metal sublayer required for CNT growth is more favorable in the Ni_3Pd at -1.27 eV (Fig. 7b' \rightarrow 7d') than the C_2 formation at -1.07 eV (Fig. 7b' \rightarrow 7d'), suggesting that buildup of carbon in the metal sublayer (i.e., the carbon required for CNT growth) is more favorable. This is also consistent with our experimental

results that show how the addition of Pd to Ni (1) stabilizes the CH₄ TCD performance and (2) favors CNT growth because the formation of the precursor for CNT growth (sub-layered C) is more energetically favorable than the formation of the coke precursor (C₂).

3.5. Preliminary Technoeconomic analysis

Preliminary Technoeconomic analysis was conducted by comparing TCD with commercial steam methane reforming with and without CO₂ capture. Major advantages of TCD are the near zero CO₂ emission and high value by-products CNT/CNF. Results are summarized in SI.

4. Conclusions

Ni and Ni-Pd alloy supported on CNT with various atomic ratios were synthesized and tested for methane TCD. It was demonstrated that the introduction of Pd significantly affected the physicochemical properties of the catalyst and formation mechanisms of carbon materials. The methane conversion and carbon yield of the catalysts were highly dependent on the Ni/Pd ratio and reaction temperature. Pure Ni catalysts deactivated within 2 hr of reaction due to graphitic carbon encapsulation. The supported and unsupported Ni-Pd alloy catalysts exhibited an improved sintering resistance and stable operation for 6 hr. An optimum Ni:Pd mass ratio between 10 and 15 was experimentally determined. DFT and MKM calculations revealed that pure Ni catalyst deactivated most likely due to preferred formation and accumulation of coke precursors (C₂) over the metal surface. However, the Ni-Pd catalysts were more stable due to

the lower energy of carbon migrating to the metal sublayer favoring CNT growth. The cyclic reaction-regeneration for self-sustained process was demonstrated by re-synthesizing the 10Ni-1Pd/CNT catalyst using the produced CNTs/CNFs as support after leaching out the metal. After five cycles of operation, the property of CNT/CNF product remained unchanged.

CRedit authorship contribution statement

I-Wen Wang: Catalyst formulation & synthesis, Characterization, Experimental, Formal Analysis, Original draft. **Robert A. Dagle:** Research collaboration, Manuscript editing. **Tuhin Suvra Khan:** DFT modeling and analysis. **Juan A. Lopez-Ruiz:** Catalyst characterization, draft review **Libor Kovarik:** Morphological analysis. **Yuan Jiang:** process simulation. **Mengze Xu:** Catalyst characterization. **Yi Wang:** Spent catalyst characterization. **Changle Jiang:** Technical discussion. **Stephen D. Davidson:** Catalyst characterization. **Pedram Tavadze:** DFT model computing. **Lili Li:** Catalyst synthesis advice, Concept development. **Jianli Hu:** Research administration, Concept development, Resources, Advisory.

Declaration of competing interest

The authors declare that they have no known competing financial interests or personal relationships that could have appeared to influence the work reported in this paper.

Acknowledgements

This work was financially supported by the U.S. Department of Energy (DOE), Office of Energy Efficiency and Renewable Energy (EERE), Fuel Cell Technologies Office (FCTO).

Funding was also provided by Southern California Gas Company (SoCalGas) and C4-MCP, Inc. as part of a cooperative research and development agreement (CRADA) project led by PNNL under CRADA No. 401. Work was performed at West Virginia University (WVU) and at Pacific Northwest National Laboratory (PNNL) under Contract DE-AC05-76R. PNNL is a multiprogram national laboratory operated for the DOE by Battelle Memorial Institute. Some STEM and elemental mapping characterization were performed at the William R. Wiley Environmental Molecular Sciences Laboratory (EMSL), which is a national scientific user facility sponsored by the DOE Office of Biological and Environmental Research and located at PNNL, under EMSL user proposal 51211. The views and opinions of the authors expressed herein do not necessarily state or reflect those of the United States Government or any agency thereof. Neither the United States Government nor any agency thereof, nor any of their employees, makes any warranty, expressed or implied, or assumes any legal liability or responsibility for the accuracy, completeness, or usefulness of any information, apparatus, product, or process disclosed or represents that its use would not infringe privately owned rights.

References

- 1 B. Parkinson, P. Balcombe, J. F. Speirs, A. D. Hawkes and K. Hellgardt, *Energy Environ. Sci.*, 2019, **12**, 19–40.
- 2 Y. Khojasteh Salkuyeh, B. A. Saville and H. L. MacLean, *Int. J. Hydrogen Energy*, 2017, **42**, 18894–18909.

- 3 T. Keipi, H. Tolvanen and J. Konttinen, *Energy Convers. Manag.*, 2018, **159**, 264–273.
- 4 N. Muradov, *Int. J. Hydrogen Energy*, 2017, **42**, 14058–14088.
- 5 P. Nikolaidis and A. Poullikkas, *Renew. Sustain. Energy Rev.*, 2017, **67**, 597–611.
- 6 Y. K. Salkuyeh, B. A. Saville and H. L. MacLean, *Int. J. Hydrogen Energy*, 2018, **43**, 9514–9528.
- 7 L. B. Avdeeva, O. V. Goncharova, D. I. Kochubey, V. I. Zaikovskii, L. M. Plyasova, B. N. Novgorodov and S. K. Shaikhutdinov, *Appl. Catal. A Gen.*, 1996, **141**, 117–129.
- 8 D. Ayillath Kutteri, I. W. Wang, A. Samanta, L. Li and J. Hu, *Catal. Sci. Technol.*, 2018, **8**, 858–869.
- 9 A. F. ad Syed Muhammad, A. Awad, R. Saidur, N. Masiran, A. Salam and B. Abdullah, *Int. J. Hydrogen Energy*, 2018, **43**, 18713–18734.
- 10 Y. Shen and A. C. Lua, *Appl. Catal. B Environ.*, 2015, **164**, 61–69.
- 11 H. F. Abbas and W. M. A. Wan Daud, *Int. J. Hydrogen Energy*, 2010, **35**, 1160–1190.
- 12 M. Pudukudy, Z. Yaakob and Z. S. Akmal, *Appl. Surf. Sci.*, 2015, **353**, 127–136.
- 13 Y. Li, B. Zhang, X. Xie, J. Liu, Y. Xu and W. Shen, *J. Catal.*, 2006, **238**, 412–424.
- 14 I. Suelves, J. L. Pinilla, M. J. Lázaro, R. Moliner and J. M. Palacios, *J. Power Sources*, 2009, **192**, 35–42.
- 15 U. P. M. Ashik, W. M. A. Wan Daud and H. F. Abbas, *Renew. Sustain. Energy Rev.*, 2015, **44**, 221–256.
- 16 L. Zhou, L. R. Enakonda, M. Harb, Y. Saih, A. Aguilar-Tapia, S. Ould-Chikh, J. Louis Hazemann, J. Li, N. Wei, D. Gary, P. Del-Gallo and J. M. Basset, *Appl. Catal. B Environ.*, 2017, **208**, 44–59.
- 17 Y. Echegoyen, I. Suelves, M. J. Lázaro, M. L. Sanjuán and R. Moliner, *Appl. Catal. A Gen.*, 2007, **333**, 229–237.
- 18 L. Alves, V. Pereira, T. Lagarteira and A. Mendes, *Renew. Sustain. Energy Rev.*, , DOI:10.1016/j.rser.2020.110465.
- 19 Z. Fan, W. Weng, J. Zhou, D. Gu and W. Xiao, *J. Energy Chem.*, 2021, **58**, 415–430.
- 20 Q. Chen and A. C. Lua, *Chem. Eng. J.*, 2020, **389**, 124366.

- 21 C. Palmer, D. C. Upham, S. Smart, M. J. Gordon, H. Metiu and E. W. McFarland, *Nat. Catal.*, 2020, **3**, 83–89.
- 22 Z. Fan and W. Xiao, *Angew. Chemie - Int. Ed.*, 2021, **60**, 7664–7668.
- 23 D. Kang, C. Palmer, D. Mannini, N. Rahimi, M. J. Gordon, H. Metiu and E. W. McFarland, *ACS Catal.*, 2020, **10**, 7032–7042.
- 24 J. Zeng, M. Tarazkar, T. Pennebaker, M. J. Gordon, H. Metiu and E. W. McFarland, *ACS Catal.*, 2020, **10**, 8223–8230.
- 25 M. A. Salam and B. Abdullah, *Mater. Chem. Phys.*, 2017, **188**, 18–23.
- 26 S. Helveg, L.-C. Carlos, J. Sehested, P. L. Hansen, B. S. Clausen, J. R. Rostrup-Nielsen, F. Abild-Pedersen and J. K. Nørskov, *Nature*, 2004, **427**, 426–429.
- 27 E. J. G. Santos, J. K. Nørskov, A. R. Harutyunyan and F. Abild-Pedersen, *J. Phys. Chem. Lett.*, 2015, **6**, 2232–2237.
- 28 S. Hofmann, G. Csányi, A. C. Ferrari, M. C. Payne and J. Robertson, *Phys. Rev. Lett.*, 2005, **95**, 1–4.
- 29 N. Shah, S. Ma, Y. Wang and G. P. Huffman, *Int. J. Hydrogen Energy*, 2007, **32**, 3315–3319.
- 30 N. Muradov, F. Smith and A. T-Raissi, *Catal. Today*, 2005, **102–103**, 225–233.
- 31 J. L. Pinilla, I. Suelves, R. Utrilla, M. E. Gálvez, M. J. Lázaro and R. Moliner, *J. Power Sources*, 2007, **169**, 103–109.
- 32 H. Hu, B. Zhao, M. E. Itkis and R. C. Haddon, *J. Phys. Chem. B*, 2003, **107**, 13838–13842.
- 33 G. Kresse and J. Furthmüller, *Comput. Mater. Sci.*, 1996, **6**, 15–50.
- 34 D. Vanderbilt, *Phys. Rev. B*, 1990, **41**, 7892–7895.
- 35 B. Hammer, L. B. Hansen and J. K. Nørskov, *Phys. Rev. B - Condens. Matter Mater. Phys.*, 1999, **59**, 7413–7421.
- 36 H. J. Monkhorst and J. D. Pack, *Phys. Rev. B*, 1976, **13**, 5188–5192.
- 37 M. Methfessel and A. T. Paxton, *Phys. Rev. B*, 1989, **40**, 3616–3621.
- 38 J. R. Sanchez-Valencia, T. Dienel, O. Gröning, I. Shorubalko, A. Mueller, M. Jansen, K. Amsharov, P. Ruffieux and R. Fasel, *Nature*, 2014, **512**, 61–64.

- 39 A. Harpale, M. Panesi and H. B. Chew, *J. Chem. Phys.*, , DOI:10.1063/1.4907716.
- 40 J. A. Elliott, Y. Shibuta, H. Amara, C. Bichara and E. C. Neyts, *Nanoscale*, 2013, **5**, 6662–6676.
- 41 A. Gili, L. Schlicker, M. F. Bekheet, O. Görke, D. Kober, U. Simon, P. Littlewood, R. Schomäcker, A. Doran, D. Gaissmaier, T. Jacob, S. Selve and A. Gurlo, *ACS Catal.*, 2019, **9**, 6999–7011.
- 42 A. Nash and P. Nash, *J. Phase Equilibria*, 1984, **5**, 446–450.
- 43 A. Martínez de Yuso, J. M. Le Meins, Y. Oumellal, V. Paul-Boncour, C. Zlotea and C. Matei Ghimbeu, *J. Nanoparticle Res.*, , DOI:10.1007/s11051-016-3682-9.
- 44 Z. Liu, X. Zhang and L. Hong, *Electrochem. commun.*, 2009, **11**, 925–928.
- 45 J. H. Hafner, M. J. Bronikowski, B. R. Azamian, P. Nikolaev, A. G. Rinzler, D. T. Colbert, K. A. Smith and R. E. Smalley, *Chem. Phys. Lett.*, 1998, **296**, 195–202.
- 46 W. He, C. Wang, H. Wang, M. Jian, W. Lu, X. Liang, X. Zhang, F. Yang and Y. Zhang, *Sci. Adv.*, 2019, **5**, 1–9.
- 47 J. L. Pinilla, I. Suelves, M. J. Lázaro, R. Moliner and J. M. Palacios, *Int. J. Hydrogen Energy*, 2010, **35**, 9801–9809.
- 48 L. Ni, K. Kuroda, L. P. Zhou, T. Kizuka, K. Ohta, K. Matsuishi and J. Nakamura, *Carbon N. Y.*, 2006, **44**, 2265–2272.
- 49 C. Lu and J. Liu, *J. Phys. Chem. B*, 2006, **110**, 20254–20257.
- 50 TUINSTRAL F and KOENIG JL, *J. Chem. Phys.*, 1970, **53**, 1126–1130.
- 51 A. J. Medford, C. Shi, M. J. Hoffmann, A. C. Lausche, S. R. Fitzgibbon, T. Bligaard and J. K. Nørskov, *Catal. Letters*, 2015, **145**, 794–807.
- 52 L. C. Grabow, *CHAPTER 1. Computational Catalyst Screening*, 2014.
- 53 S. Takenaka, Y. Shigeta, E. Tanabe and K. Otsuka, *J. Catal.*, 2003, **220**, 468–477.
- 54 A. S. Al-Fatesh, A. H. Fakeeha, W. U. Khan, A. A. Ibrahim, S. He and K. Seshan, *Int. J. Hydrogen Energy*, 2016, **41**, 22932–22940.
- 55 I. Suelves, M. J. Lázaro, R. Moliner, B. M. Corbella and J. M. Palacios, *Int. J. Hydrogen Energy*, 2005, **30**, 1555–1567.
- 56 M. Losurdo, M. M. Giangregorio, P. Capezzuto and G. Bruno, *Phys. Chem. Chem. Phys.*, 2011, **13**, 20836–20843.

- 57 F. Abild-Pedersen, J. K. Nørskov, J. R. Rostrup-Nielsen, J. Sehested and S. Helveg, *Phys. Rev. B - Condens. Matter Mater. Phys.*, 2006, **73**, 1–13.